Nanoscale Advances

PAPER

View Article Online
View Journal | View Issue

Cite this: *Nanoscale Adv.*, 2023, **5**, 685

Revealing the alloying and dealloying behaviours in AuAg nanorods by thermal stimulus†

Long-Bing He, *[ab] Lei Shangguan,[a] Ya-Ting Ran,[a] Chao Zhu,[a] Zi-Yu Lu,[a] Jiong-Hao Zhu,[a] Dao-Jiang Yu,[a] Cai-Xia Kan *[c] and Li-Tao Sun [ab]

Binary metallic nanocrystals are attractive as they offer an extra degree of freedom for structure and phase modulation to generate synergistic effects and extraordinary properties. However, whether the binary structures and phases at the nanoscale still follow the rules established on the bulk counterparts remains unclear. In this work, AuAg nanorods were used as a sample to probe into this issue. An *in situ* heating method by combining aberration-corrected transmission electron microscopes with a chip-based heating holder was employed to perform the heating experiments. It was found that the AuAg nanorods, which initially possessed heterostructures, can be designed and engineered to be gradient phase alloys with thermal pulses over 350 °C. Atomic diffusion inside the rod structures did not alter the shape of the rods but provided a route to fine-tune their properties. At higher temperatures, the discrepant sublimation behaviours between Au and Ag lead to dealloying of the nanorods. Durative sublimation of the Ag element can continuously tailor the lengths of the nanorods while concentrating the Au composition simultaneously. Especially, nearly pure Au nanocrystals can be obtained with the depletion of Ag by sublimation. These findings give insights into the nanoscale structure and phase behaviours in binary alloys and provide an alternative way to fine-tune their structure, phase, and properties.

Received 26th October 2022
Accepted 7th December 2022

DOI: 10.1039/d2na00746k

rsc.li/nanoscale-advances

1. Introduction

Bimetallic nanocrystals have attracted great interest as they offer an extra degree of freedom to fine-tune their structures, phases, and properties in comparison with the elemental ones. Diverse configurations and synergistic effects can be obtained in these nanocrystals, which frequently enable novel functionalities facilitating diverse applications including optics,[1–6] plasmonics,[7–12] catalysis,[13–20] sensors,[21–28] and biomedicine.[29–33] For example, Xu *et al.* have reported that bimetallic AuAg core–shell catalysts show much higher catalytic activity than elemental Au and Ag catalysts in reducing 4-nitrophenol.[17] Huang *et al.* have demonstrated that the PtPd nanocrystals are active in the hydrogenation of nitrobenzene, while their catalytic performances depend on the nanocrystal shape, facet, and composition strongly.[16] Yuan *et al.* fabricated a fluorescence-and-Raman sensor based on assembled AuAg nanorods, and an extreme detection limit of 0.007 ng mL^{-1} for Hg was achieved with this sensor, which is much better than most of the sensors based on other technologies.[27] Wang *et al.* have demonstrated a significant synergistic effect in the NiCo bimetallic nanocrystals, and this synergistic effect enables a much better catalytic performance of ultrafine NiCo catalyst than individual Ni or Co in the hydrogenation process from furfuryl alcohol to tetrahydrofurfuryl alcohol.[34] Xiong *et al.* have demonstrated a better performance of bimetallic PdPt catalysts over pure Pd or Pt nanocrystals in the semi-hydrogenation process.[35] Despite the extraordinary properties and performance, Ni *et al.* also demonstrate that alloyed AuAg nanorods exhibit improved thermal stability when they are used as Raman substrates in harsh environments.[36] Based on all these achievements, it can be found that the extraordinary properties of bimetallic nanocrystals are closely related to their structures and phases. Although multifarious shapes and configurations can be synthesized *via* delicate chemical methods, the yielded bimetallic nanocrystals frequently stay in metastable states and suffer further shape/phase evolution when they undergo practical applications. This often brings reliability issues to products and may further cause low efficiency or even functionality failure.

Pertaining to this issue, it is of critical importance to reveal the structure and phase behaviours of metallic nanocrystals to provide fundamental instructions for property modulation together with stability estimation. Unfortunately, as the crystal size decreases to the nanometer scale, the size effect and surface effect become more and more prominent and whether the

[a]SEU-FEI Nano-Pico Center, Key Laboratory of MEMS of Ministry of Education, Southeast University, Nanjing 210096, P. R. China. E-mail: helongbing@seu.edu.cn
[b]Centre for Advanced Materials and Manufacture, Joint Research Institute of Southeast University and Monash University, Suzhou 215123, P. R. China
[c]College of Physics, Nanjing University of Aeronautics and Astronautics, No. 29 Jiangjun Road, Nanjing 211106, P. R. China. E-mail: cxkan@nuaa.edu.cn

† Electronic supplementary information (ESI) available. See DOI: https://doi.org/10.1039/d2na00746k

theories established based on the bulk materials can still be valid on the nanocrystals is currently uncertain. Some pioneering investigations have uncovered some differences between nanoalloys and their bulk counterparts. For example, the phase diagrams of PbBi[37] and AuGe[38] nanoalloys are found to require modifications relating to their dimensional sizes. The energy-preferable configurations of AgCu,[39] AuCu,[40] and CuNi[41] nanocrystals are found to depend on particle sizes, surface segregations, and temperatures strongly. However, the obtained results usually show case-by-case scenarios in different bimetallic systems. There is still a lack of universal law to describe their behaviours and properties. Therefore, extensive research is still required to gain a comprehensive understanding of the property and stability of bimetallic nanocrystals. In this work, AuAg nanorods were used as a sample to perform an investigation on this issue. An *in situ* heating approach was employed by combining heating holders with aberration-corrected transmission electron microscopes (TEMs) and energy dispersive spectroscopy (EDS). This method enables a direct observation and identification of the structure and phase evolution of the nanorods under different stimuli, which can provide illuminating insights into their intrinsic property, stability, and the mechanisms lying behind them.

2. Experimental

2.1 Sample preparation and characterization

The AuAg nanorods were synthesized by a chemical method and stored in deionized water.[42] Aberration-corrected TEMs (FEI Titan 80-300 and JEM ARM200F) were used to perform structure and EDS characterization. The dark-field images were acquired with a high-angle annular detector in the scanning-TEM (STEM) mode using the probe-corrected ARM200F TEM. The dynamic videos and bright-field images were acquired with the image-corrected Titan 80-300 TEM. A frame ratio of 3 fps was used to capture the dynamic evolution during sublimation. Especially, to form thin carbon shells on the AuAg nanorods, the samples were initially irradiated by the electron beam at low magnifications for several minutes.[43,44] This step allowed the decomposition of hydrocarbon molecules adsorbed on the sample before they were evaporated during heating. As a result, thin carbon layers were deposited on the AuAg nanorods to form core–shell structures (see more details in the ESI†).

2.2 *In situ* heating

The heating experiments were carried out using a thermoelectric holder Fusion ST350 from the Protochips Company. AuAg nanorods were dispersed onto an electrical heating chip first, and then the chip was mounted onto the holder. After that, the holder was inserted into the TEM chamber for further characterization. The heating chip enables a nominal ramping rate of 1000 °C ms^{-1} from room temperature to 1200 °C. The heating process was programmed using the software. In the pulse heating mode, the low-temperature T_1 was set at room temperature, while the high-temperature T_2 was set to be the targeted temperature. In a typical heating pulse, the sample was heated from T_1 to T_2 directly and maintained for a certain while (duration time), and then cooled to T_1.

3. Results and discussion

Fig. 1a shows the bright-field TEM image of the typical as-synthesized AuAg nanorods. The nanorods have diameters of 25–30 nm and lengths of 70–400 nm in general. Because the AuAg nanorods are synthesized *via* the epitaxial growth of Ag over bipyramid Au seeds,[42] their structures present a clear feature that the Au cores are in the middle while the Ag are grown symmetrically along the two sides. Benefiting from the well-purified seed size, the Au cores in the AuAg nanorods are highly homogenous, despite that different Ag extensions are designed and regrown. Fig. 1b shows the dark-field image of the AuAg nanorods obtained *via* the STEM mode. Due to the distinct *Z*-contrasts between Au and Ag, the heterostructures can be identified apparently from the STEM images. It can be seen that the epitaxial growth of Ag on the Au seeds almost maintains the initial diameter of the Au seeds, forming sharp heterointerfaces and atomically smooth nanorod surfaces. Fig. 1c–e show the high-resolution S/TEM images at the interfaces of a long nanorod and a short nanorod. The crystalline orientations match perfectly, and no visible interdiffusion was found (Fig. S1 and S2†).

The long AuAg nanorods were selected to perform the heating treatments. Fig. 2a shows the STEM image of the initial AuAg heterostructures with sharp Au–Ag interfaces illustrated in the inset. The thermal pulses were set at 450 °C with a duration time of 1 s for each pulse. It means that the AuAg nanorods were heated from room temperature to 450 °C and lasted for 1 s before cooling down to room temperature again. Short duration times are set for the thermal pulses in order to slow down the structure/phase evolution to enable close monitoring. Fig. 2b shows the structure change after exerting a few thermal pulses. As can be seen, the boundary in *Z*-contrast between Au and Ag becomes blurry after this treatment, indicating that interdiffusion should have taken place in the nanorods under the stimulus of thermal pulses. Nevertheless, the nanorod shapes were well maintained during this interdiffusion-induced alloying process. As shown in Fig. S3,† the alloying process takes more than 23 thermal pulses (450 °C) to enable a better solid solution phase. With further interdiffusion, the contrast difference between the Au-rich part and the Ag-rich part becomes slighter and slighter. It hence brings difficulty in further estimation of the structural changes from the STEM images even with more thermal pulses. To accelerate the diffusion in each step, a single AuAg nanorod was examined by exerting thermal pulses with increasing heating temperatures. The duration times of the thermal pulses were still set as 1 s, but the target temperatures were increased by 30 °C per step after each thermal pulse. Fig. 2c and d show the structure/phase evolution tracked after each thermal pulse. It can be seen that the Au core disperses significantly at elevated temperatures. Together with the dispersion of the Au core, the brightness of the rod ends was also enhanced, implying the occurrence of alloying. This conclusion was further evidenced by performing

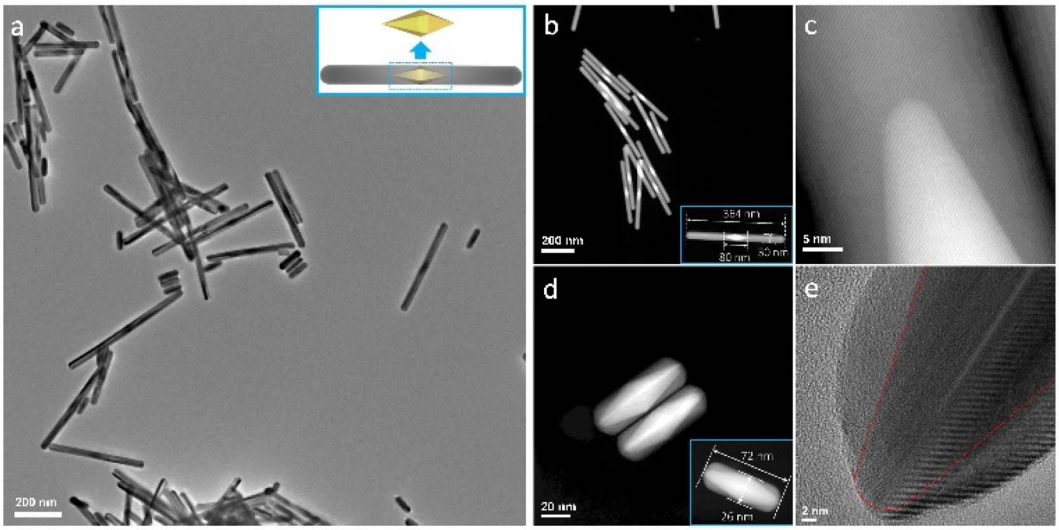

Fig. 1 (a) Bright-field TEM image of the as-synthesized AuAg nanorods. The inset is the illustration of the heterostructure. (b) Dark-field STEM images of typical AuAg nanorods. The brighter cores are Au while the lighter parts are Ag. The insets show the lengths and diameters of typical samples. (c) High-resolution STEM image showing the crystalline Au–Ag interface of a long nanorod. (d, e) High-resolution STEM and TEM images showing the Au–Ag interface of a short nanorod. The crystalline orientations match perfectly. More details can be found in ESI Fig. S1 and S2.†

the EDS measurements. As shown in Fig. 2e–g, the EDS spectra obtained at the middle point and one end of the nanorod presented almost the same peak intensities. Both the Ag and Au signals were observed in the spectra. This corroborates that an even alloy phase was finally formed from the initial heterostructure.

On the evolution of the Au–Ag heterointerfaces, moderate thermal pulses are preferred to slow down the interdiffusion process. Fig. 2h shows an atomic-resolution STEM image of the initial heterointerface of another AuAg nanorod. Perfect twin structures can be identified along this view direction, as the nanorods have a five-fold symmetry.[42] With a thermal pulse of 350 °C for 1 s, as shown in Fig. 2i, the sharp Au–Ag heterointerface turns to be fuzzy apparently, while the profile of the Au core is still identifiable (Fig. S4 and S5†). Another thermal pulse of 380 °C for 1 s significantly boosts the interfacial diffusion (Fig. 2j). The Au core is quite blurry and only a gradient contrast can be identified. Moreover, a further thermal pulse of 450 °C for 1 s flattens the contrast gradient in this observation region, as shown in Fig. 2k. During this diffusion process, no special diffusion channel was observed, though the pentagonal structure provides some grain/twin boundaries where we expect to find some early diffusion phenomenon. The nearly even contrast in Fig. 2k suggests an isotropic diffusion fashion inside the nanorod.

Besides the atomistic structures, EDS line scans were also performed on the AuAg nanorod during each of the thermal pulses. As shown in Fig. 3, half of the nanorod was monitored and all the line scans were performed using the same parameters. In the initial stage, the EDS line scan (Fig. 3b) exhibited a slope corresponding to the bipyramid Au core and a sharp boundary at the Au–Ag interface. The signal of Au decreases to zero from this boundary to the far end. After the thermal pulses were exerted, the extensions of the Au signal could be distinctly observed, as indicated by the shadow regions marked in Fig. 3d, f, h, j and l. Meanwhile, the Ag signals in these shadow regions enhanced steadily due to the reversed diffusion. It shows that a higher temperature leads to a longer composition gradient of the Au. Especially in Fig. 3h, j and l, the stepwise increases of the Au signal at the nanorod end corroborated the continuous alloying process under more thermal pulses. Due to the limits of EDS sensitivity and resolution, it is still unable to track the diffusion channels at the atomic scale. Nevertheless, the diffusion trend of the Au atoms suggests that an even alloying phase can be obtained with sufficient thermal pulses. It should also be noted that the Ag signal scatters in the region near the nanorod end after exerting the thermal pulses over 570 °C. This indicates that even using this discrete heating mode, high temperatures over around 570 °C may give rise to some sublimation of Ag. Therefore, for the purpose of fine-tuning the phase without influencing the nanorod shape, low temperatures are preferred to avoid structural damage.

Since the Au–Ag alloy maintains a solid-solution phase as their thermodynamic equilibrium phase,[45] the AuAg nanorods will retain their alloying structures after thermal treatments without a further phase evolution. That is, further structure and phase modulation will be infeasible in this situation. However, the discrepant vapour pressures between Au and Ag actually provide an extra way to further fine-tune the structure and phase if partial damages of the nanorods are accepted. The prior sublimation of Ag at appropriate temperatures may provide an effective approach to concentrating the Au composition, yielding shortened nanorods with adjustable Au/Ag compositional ratios. Fig. 4a shows the implementation of Ag sublimation by exerting thermal pulses of 780 °C with a duration time of 0.5 s. Although a temperature of ~690 °C already can cause

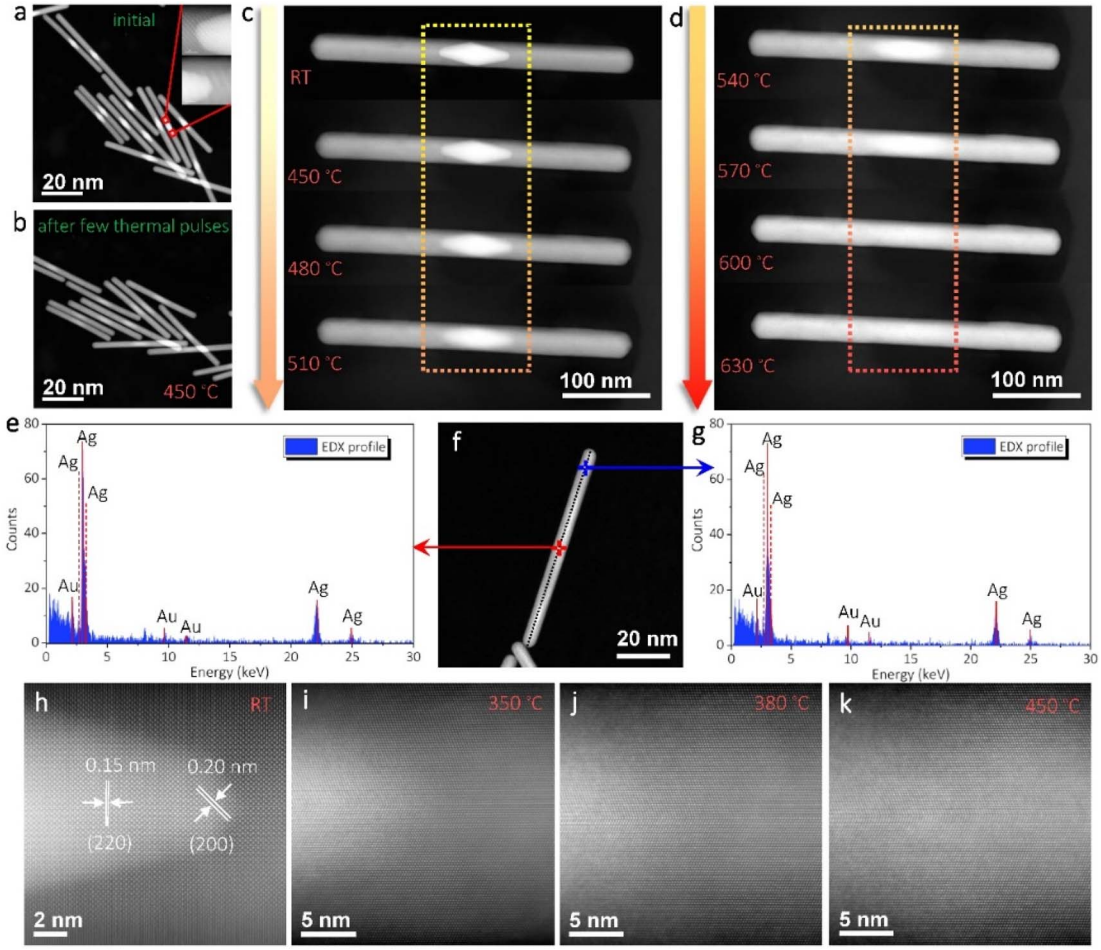

Fig. 2 (a) Dark-field STEM image of the initial AuAg nanorods at room temperature. The inset shows the interfaces of a typical nanorod. (b) Dark-field STEM image of the AuAg nanorods after exerting a few thermal pulses. The thermal pulse is set as 450 °C with a duration time of 1 s. (c and d) STEM image sequences showing the alloying process of a typical AuAg nanorod. The duration time of each thermal pulse is 1 s while the target temperature is increased from 450 °C to 630 °C with 30 °C per step. (e–g) EDS measurements of a typical AuAg nanorod after alloying. The EDS spectra in (e and g) are measured at the rod middle and the rod end, respectively. (h–k) Atomic-resolution STEM images showing the evolution of the Au–Ag interfacial region under thermal pulses: (h) the initial state; (i) after a thermal pulse of 350 °C for 1 s; (j) after an extra thermal pulse of 380 °C for 1 s; (k) after a further thermal pulse of 450 °C for 1 s.

significant sublimation in a continuous heating mode (Video S1†), the selection of a higher temperature pulse with a shorter duration period was tried here to make a distinct structural change during each thermal pulse. As can be seen, sublimation occurs from a weak point and forms a groove on the nanorod surface. With further sublimation, the groove enlarges and the nanorod is divided into two segments. With the continuous decrease of the two segments under each thermal pulse, they finally turn into two nanoparticles and seem to stay stable. In this period, the nanoparticles sublimate very slowly and their size change is almost imperceptible. Fig. 4b and d show another two nanorods under sublimation. The corresponding high-resolution STEM images in Fig. 4c and e, clearly demonstrate that the nanorods retain crystalline structures during sublimation. Moreover, the crystal orientations are also maintained similar to what the nanorods initially possessed. Fig. 4f shows the EDS mappings of the nanorod segments during sublimation in stages vii, viii, and ix. Obviously, the segments mostly maintained the solid-solution phase, with the Au signal (in red) and Ag signal (in green) evenly distributed. When the Ag is about to run out (stage ix), the Ag signal weakens significantly while the Au signal remained strong.

Although it still lacks an accurate description of the sublimation behaviour of solid-solution alloys, the observed phenomena here may be roughly estimated by the individual vapour pressures of Au and Ag (Fig. S6†). Because Ag has a much higher saturation vapour pressure than that of Au (*e.g.* 3–4 orders at 780 °C), it seems reasonable to infer that pure Au can be obtained by sufficient sublimation of the Ag composition. This strategy should be universal to all the AuAg nanorods, and can be used to adjust the optical properties of the structures, such as plasmonic resonance, from an Ag-rich style to a fully Au-dominant one.

It should be noted that the maintenance of the rod shape during sublimation is due to the existence of thin carbon shells on the AuAg samples. The carbon shells are mostly formed by

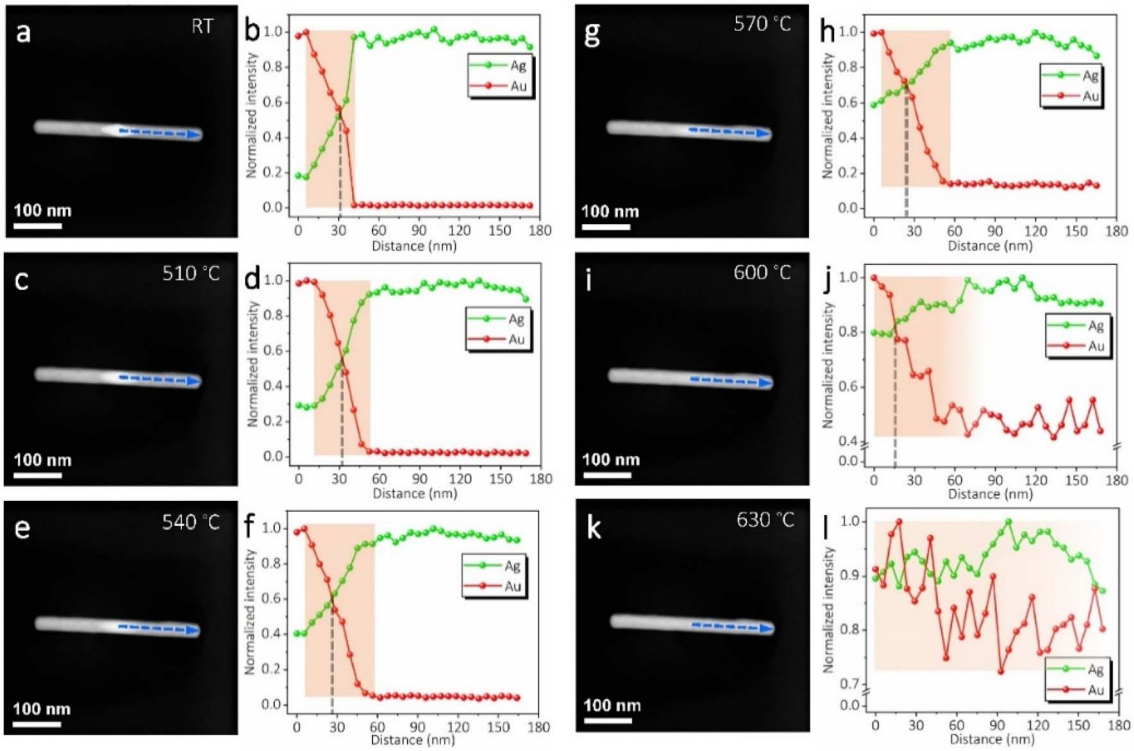

Fig. 3 Dark-field STEM images and corresponding EDS line scans of the AuAg nanorod under different thermal pulses. (a and b) Initial state. (c and d) After a thermal pulse of 510 °C for 1 s. (e and f) After a further thermal pulse of 540 °C for 1 s. (g and h) After a further thermal pulse of 570 °C for 1 s. (i and j) After a further thermal pulse of 600 °C for 1 s. (k and l) After a further thermal pulse of 630 °C for 1 s. The EDS intensities are normalized with the highest value to be 1. They reflect the relative elemental distributions in each case.

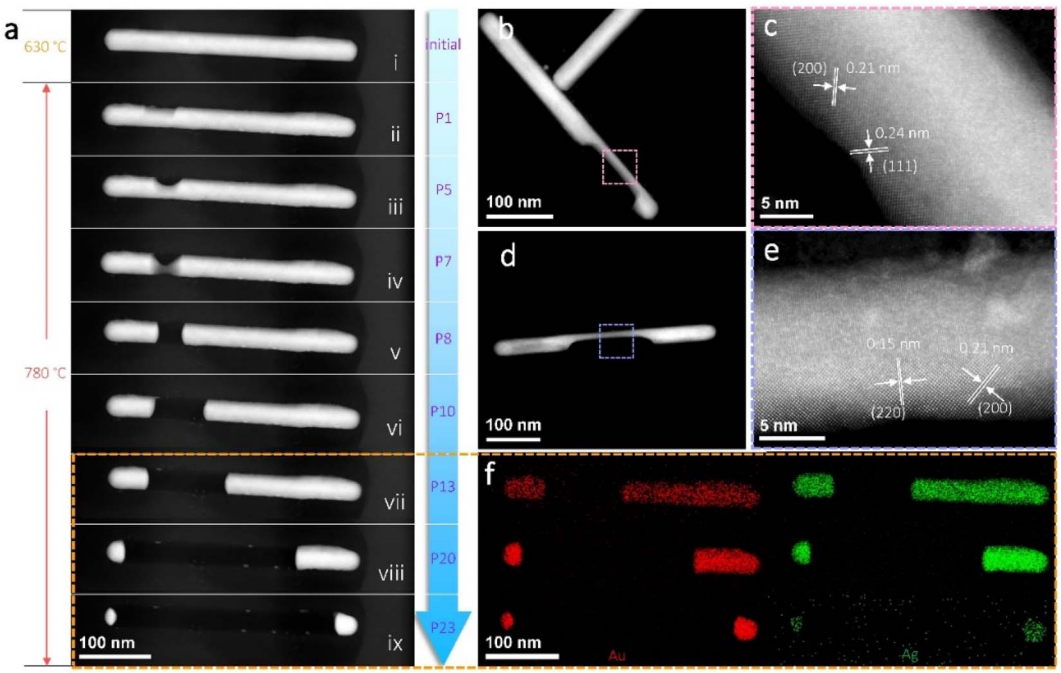

Fig. 4 (a) Dark-field STEM image sequence showing the morphology evolution of a AuAg nanorod under thermal pulses (780 °C with a duration time of 0.5 s for one thermal pulse). i to ix indicate the sublimation stages of the AuAg nanorod under different thermal pulses. The number of thermal pulses is marked in the blue band. (b–e) Morphologies and corresponding crystalline structures of two AuAg nanorods during sublimation. The high-resolution STEM images in (c and e) demonstrate that the nanorods maintain their crystal orientations and monocrystalline structures. (f) EDS mappings of the AuAg nanorod in stages vii to ix in (a).

electron beam-induced decomposition of residual surfactant molecules, which are induced during chemical synthesis. These carbon shells can largely prevent surface instability and reshaping of the AuAg nanorods when they are heated at elevated temperatures. As a result, sublimation only gives rise to the decrease of nanorod length without sintering/coalescing into large particles. To further reveal this sublimation-induced concentration phenomenon, a bundle of AuAg nanorods was heated to 720 °C and their shape evolutions were tracked in real-time. As shown in Fig. 5a, all the nanorods underwent apparent sublimation at this temperature. Due to the confinement of carbon shells, the nanorods shrink from one end to the opposite end or from middle positions towards their two ends depending on the first break points created by sublimation-induced pressure accumulation. Constant sublimation takes place in all the nanorods until they reach certain sizes, as marked by the dashed circles and columns. Finally, nanoparticles and short nanorods are left without significantly observable sublimation.

Fig. 5b and Video S2† give more details of the dynamic sublimation process by tracking five AuAg nanorods, which have several connections with each other. The dark-field STEM image shows their initial morphology, while the bright-field TEM images show the dynamic evolution during sublimation. As can be seen, even though nanorod-ii sublimates later than the other nanorods, all five nanorods turn into nanoparticles eventually after sufficient sublimation. Interestingly, due to the connections among nanorods-i, ii, iii, and iv, the Au and Ag atoms are able to diffuse along the nano-channels, leading to an empty carbon tube (nanorod-i) and significantly larger nanoparticles inside the carbon tube (nanorod-ii). In contrast, the isolated nanorod-v turns into two small nanoparticles on the two ends. Fig. 5c shows the results of the nanorod network after sublimation. In this region, more empty carbon tubes and much larger residual nanoparticles are observed. This indicates that strong diffusion and fusion have taken place due to the existence of more connection channels. Moreover, the EDS spectrum proves that the residual nanoparticles are nearly pure Au. At this stage, if the heating temperature is further improved, *e.g.* over 850 °C, very slow sublimation/evaporation may be identified. A distinct decrease in nanoparticle size may take several minutes, which is much longer than that of AuAg sublimation.

The alloying and dealloying phenomena not only give information for the phase behaviours of AuAg nanocrystals but also provide experimental evidence for examining the validity of using the phase behaviour to derive other properties. For example, Chmielewski *et al.* calculated the surface energy of the AuCu nanocrystals by fitting their size evolution curve during sublimation with Kelvin's equation.[46] The basis of this method is supposing that the AuCu can maintain a certain Au/Cu composition ratio during continuous sublimation. Thereby,

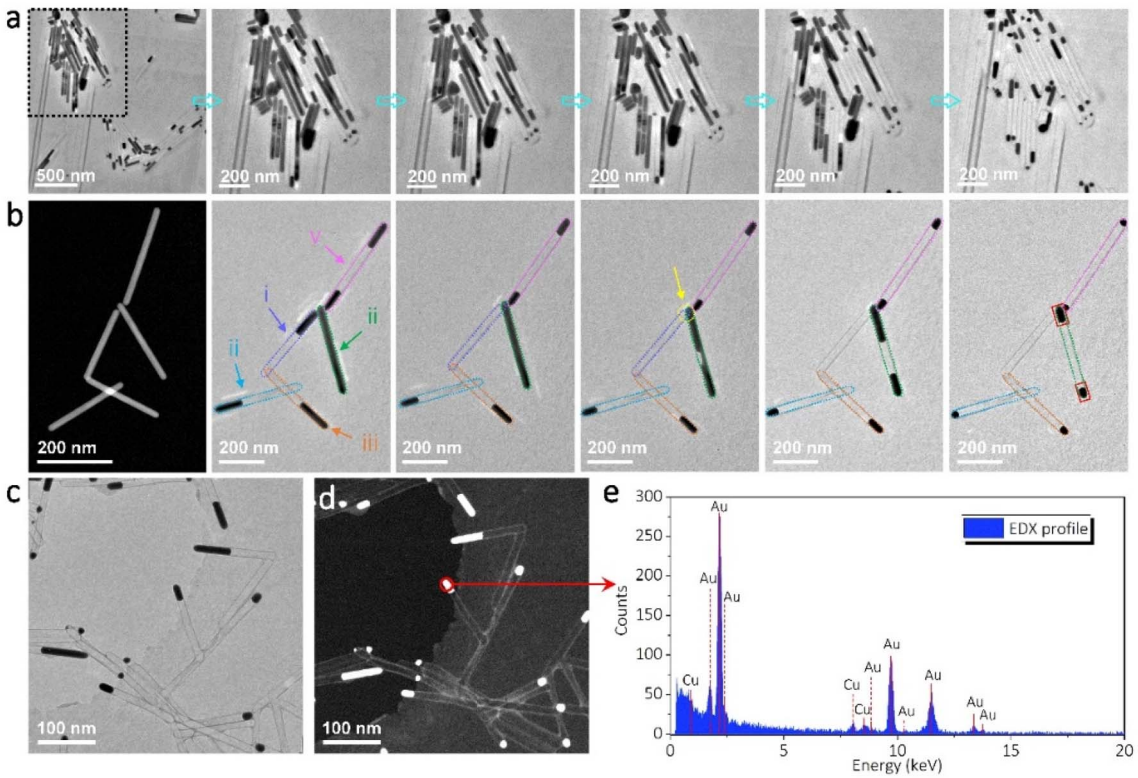

Fig. 5 (a) Image sequence showing the sublimation of a bundle of AuAg nanorods at 720 °C. All the nanorods turn into different nanoparticles. (b) Dark-field STEM and bright-field TEM images show the dynamic morphology evolution of five AuAg nanorods with some connections between each other. (c and d) Bright-field and dark-field images of a nanorod network after sublimation at 720 °C. (e) EDS spectrum of a typical residual nanoparticle marked in (d).

the sublimation behaviour reflects the property of these specified $AuCu_x$ nanocrystals, and a corresponding surface energy value is derived. However, from the vapour pressures of individual Cu and Au, this hypothesis that the $AuCu_x$ can maintain a fixed composition ratio is actually facing great challenges because the vapour pressure of Cu is about 25 times higher than that of Au at the temperatures they have used in the experiments. According to the findings herein, it is believed that similar dealloying and Au concentrations will also occur in the AuCu bimetallic system. Thus, the sublimation-induced size evolution process actually comprises a change of phase, no longer standing for a specific $AuCu_x$ nanocrystal. The derived surface energy value by fitting the sublimation curve is then inaccurate.

4. Conclusions

In summary, AuAg nanorods were used as an example to investigate the structure and phase behaviours in bimetallic nanocrystals. A combinatorial method by combining a chip-based heating holder with aberration-corrected TEMs was used to apply thermal treatments together with *in situ* observation. Different thermal pulses were exerted on the AuAg nanorods, and their structure and phase evolutions were closely monitored and analyzed. It was found that the initial hetero-structured AuAg nanorods can be designed and engineered to be nanoalloys with gradient phases under thermal pulses over 350 °C. Long-time thermal treatments of the AuAg nanorods will lead to fully alloyed structures with an even solid-solution phase. At higher temperatures (*e.g.* over 570 °C), selective sublimation occurs and the alloy nanorods change their lengths together with composition ratios. The prior sublimation of Ag leads to the concentration of Au with shortened nanorods. Nearly pure Au nanorods/nanoparticles can be obtained after the depletion of Ag. This work provides an experimental examination of the structure and phase behaviours of the AuAg bimetallic nanocrystals, which can shed some light not only on the stability estimation but also on the structure/property modulation.

Author contributions

L. H. and C. K. proposed the project. L. S., Y. R., and C. Z. conducted sample preparation and TEM experiments. L. S., D. Y., and L. H. performed data analyses. All the authors contributed to the discussion of the results. L. H. and L. S. organized and wrote the manuscript. All authors have given approval for the final version of the manuscript.

Conflicts of interest

There are no conflicts to declare.

Acknowledgements

This work is supported by the National Natural Science Foundation of China (Grant No. 52071077 and 12274072), and the Fundamental Research Funds for the Central Universities. L. H. gives special thanks to the Center for Atomic Layer Deposition and Etching.

Notes and references

1 Y. Bu and S. Lee, *ACS Appl. Mater. Interfaces*, 2012, **4**, 3923.
2 B. Khlebtsov, V. Khanadeev and N. Khlebtsov, *Nano Res.*, 2016, **9**, 2303.
3 M. Li, Z. S. Zhang, X. Zhang, K. Y. Li and X. F. Yu, *Opt. Express*, 2008, **16**, 14288.
4 Y. Y. Ma, W. Y. Li, E. C. Cho, Z. Y. Li, T. K. Yu, J. Zeng, Z. X. Xie and Y. N. Xia, *ACS Nano*, 2010, **4**, 6725.
5 Y. C. Tsao, S. Rej, C. Y. Chiu and M. H. Huang, *J. Am. Chem. Soc.*, 2014, **136**, 396.
6 X. Wang, R. Wang, L. Shi and J. Sun, *Small*, 2015, **11**, 4737.
7 K. S. B. De Silva, A. Gentle, M. Arnold, V. J. Keast and M. B. Cortie, *J. Phys. D: Appl. Phys.*, 2015, **48**, 215304.
8 R. Jiang, H. Chen, L. Shao, Q. Li and J. Wang, *Adv. Mater.*, 2012, **24**, OP200.
9 O. Pena-Rodriguez, P. Diaz-Nunez, G. Gonzalez-Rubio, V. Manzaneda-Gonzalez, A. Rivera, J. M. Perlado, E. Junquera and A. Guerrero-Martinez, *Sci. Rep.*, 2020, **10**, 5921.
10 M. Schwartzkopf, A. Rothkirch, N. Carstens, Q. Chen, T. Strunskus, F. C. Löhrer, S. Xia, C. Rosemann, L. Bießmann, V. Körstgens, S. Ahuja, P. Pandit, J. Rubeck, S. Frenzke, A. Hinz, O. Polonskyi, P. Müller-Buschbaum, F. Faupel and S. V. Roth, *ACS Appl. Nano Mater.*, 2022, **5**, 3832.
11 L. H. Yao, J. P. Zhang, H. W. Dai, M. S. Wang, L. M. Zhang, X. Wang and J. B. Han, *Nanoscale*, 2018, **10**, 12695.
12 K. Yu, G. You, L. Polavarapu and Q.-H. Xu, *J. Phys. Chem. C*, 2011, **115**, 14000.
13 M. R. Ball, K. R. Rivera-Dones, E. B. Gilcher, S. F. Ausman, C. W. Hullfish, E. A. Lebrón and J. A. Dumesic, *ACS Catal.*, 2020, **10**, 8567.
14 A. Dutta, I. Z. Montiel, R. Erni, K. Kiran, M. Rahaman, J. Drnec and P. Broekmann, *Nano Energy*, 2020, **68**, 104331.
15 L. Hu, M. C. Dietl, C. Han, M. Rudolph, F. Rominger and A. S. K. Hashmi, *Angew. Chem., Int. Ed.*, 2021, **60**, 10637.
16 X. Huang, Y. Li, Y. Li, H. Zhou, X. Duan and Y. Huang, *Nano Lett.*, 2012, **12**, 4265.
17 H. L. Jiang, T. Akita, T. Ishida, M. Haruta and Q. Xu, *J. Am. Chem. Soc.*, 2011, **133**, 1304.
18 T.-S. Kim, J. Kim, H. C. Song, D. Kim, B. Jeong, J. Lee, J. W. Shin, R. Ryoo and J. Y. Park, *ACS Catal.*, 2020, **10**, 10459.
19 Y. Ma, K. Kobayashi, Y. Cao and T. Ohno, *Appl. Catal., B*, 2019, **245**, 681.
20 C. Wang, H. G. Yin, R. Chan, S. Peng, S. Dai and S. H. Sun, *Chem. Mater.*, 2009, **21**, 433.
21 P. C. Chen, J. Y. Ma, L. Y. Chen, G. L. Lin, C. C. Shih, T. Y. Lin and H. T. Chang, *Nanoscale*, 2014, **6**, 3503.
22 G. Li, X. Wang, L. Yan, Y. Wang, Z. Zhang and J. Xu, *ACS Appl. Mater. Interfaces*, 2019, **11**, 26116.
23 S. Lin, W. Hasi, X. Lin, S. Han, T. Xiang, S. Liang and L. Wang, *ACS Sens.*, 2020, **5**, 1465.

24 W. Liu, D. Gu and X. Li, *ACS Appl. Mater. Interfaces*, 2021, **13**, 20336.
25 T. D. Thanh, J. Balamurugan, H. V. Hien, N. H. Kim and J. H. Lee, *Biosens. Bioelectron.*, 2017, **96**, 186.
26 J. Yu, Y. Ma, C. Yang, H. Zhang, L. Liu, J. Su and Y. Gao, *Sens. Actuators, B*, 2018, **254**, 182.
27 A. Yuan, X. Wu, X. Li, C. Hao, C. Xu and H. Kuang, *Small*, 2019, **15**, e1901958.
28 W. Zhao, T. Rovere, D. Weerawarne, G. Osterhoudt, N. Kang, P. Joseph, J. Luo, B. Shim, M. Poliks and C. J. Zhong, *ACS Nano*, 2015, **9**, 6168.
29 V. Bernard, O. Zobač, J. Sopoušek and V. Mornstein, *J. Cancer Res.*, 2014, **2014**, 1.
30 X. Jiang, L. Wang, Y. Ji, J. Tang, X. Tian, M. Cao, J. Li, S. Bi, X. Wu, C. Chen and J. J. Yin, *Small*, 2017, **13**, 1602855.
31 V. Karthika, A. Arumugam, K. Gopinath, P. Kaleeswarran, M. Govindarajan, N. S. Alharbi, S. Kadaikunnan, J. M. Khaled and G. Benelli, *J. Photochem. Photobiol., B*, 2017, **167**, 189.
32 J. Li, H. Heng, J. Lv, T. Jiang, Z. Wang and Z. Dai, *Small*, 2019, **15**, e1901506.
33 M. Yang, F. Lu, T. Zhou, J. Zhao, C. Ding, A. Fakhri and V. K. Gupta, *J. Photochem. Photobiol., B*, 2020, **212**, 112025.
34 H. Wang, X. Li, X. Lan and T. Wang, *ACS Catal.*, 2018, **8**, 2121.
35 M. Li, N. Zhang, R. Long, W. Ye, C. Wang and Y. Xiong, *Small*, 2017, **13**, 1604173.
36 Y. Ni, C. Kan, L. He, X. Zhu, M. Jiang and D. Shi, *Photonics Res.*, 2019, **7**, 558.
37 W. A. Jesser, R. Z. Shneck and W. W. Gile, *Phys. Rev. B: Condens. Matter Mater. Phys.*, 2004, **69**, 144121.
38 H. Lu and X. Meng, *Sci. Rep.*, 2015, **5**, 11263.
39 L. Tang, W. Wu, L. He, K. Yu, T. Xu, Q. Zhang, L. Zhang and L. Sun, *J. Phys. Chem. Lett.*, 2019, **10**, 1973.
40 G. Guisbiers, S. Mejia-Rosales, S. Khanal, F. Ruiz-Zepeda, R. L. Whetten and M. Jose-Yacaman, *Nano Lett.*, 2014, **14**, 6718.
41 G. Guisbiers, S. Khanal, F. Ruiz-Zepeda, J. Roque de la Puente and M. Jose-Yacaman, *Nanoscale*, 2014, **6**, 14630.
42 X. Zhu, X. Zhuo, Q. Li, Z. Yang and J. Wang, *Adv. Funct. Mater.*, 2016, **26**, 341.
43 L. B. He, L. Zhang, X. D. Tan, L. P. Tang, T. Xu, Y. L. Zhou, Z. Y. Ren, Y. Wang, C. Y. Teng, L. T. Sun and J. F. Nie, *Small*, 2017, **13**, 1700743.
44 R. Lian, H. Yu, L. He, L. Zhang, Y. Zhou, X. Bu, T. Xu and L. Sun, *Carbon*, 2016, **101**, 368.
45 J. Park and J. Lee, *CALPHAD: Comput. Coupling Phase Diagrams Thermochem.*, 2008, **32**, 135.
46 A. Chmielewski, J. Nelayah, H. Amara, J. Creuze, D. Alloyeau, G. Wang and C. Ricolleau, *Phys. Rev. Lett.*, 2018, **120**, 025901.